ADVANCED MATERIALS
www.advmat.de

Piezoelectricity across 2D Phase Boundaries

Anand B. Puthirath, Xiang Zhang, Aravind Krishnamoorthy, Rui Xu, Farnaz Safi Samghabadi, David C. Moore, Jiawei Lai, Tianyi Zhang, David E. Sanchez, Fu Zhang, Nicholas R. Glavin, Dmitri Litvinov, Robert Vajtai, Venkataraman Swaminathan, Mauricio Terrones, Hanyu Zhu,* Priya Vashishta,* and Pulickel M. Ajayan**

Piezoelectricity in low-dimensional materials and metal–semiconductor junctions has attracted recent attention. Herein, a 2D in-plane metal–semiconductor junction made of multilayer 2H and 1T′ phases of molybdenum(IV) telluride ($MoTe_2$) is investigated. Strong piezoelectric response is observed using piezoresponse force microscopy at the 2H–1T′ junction, despite that the multilayers of each individual phase are weakly piezoelectric. The experimental results and density functional theory calculations suggest that the amplified piezoelectric response observed at the junction is due to the charge transfer across the semiconducting and metallic junctions resulting in the formation of dipoles and excess charge density, allowing the engineering of piezoelectric response in atomically thin materials.

1. Introduction

Since the discovery of piezoelectricity in 1880 by J. Curie and P. Curie, there has been a constant search for materials capable of showing piezoelectricity where mechanical stress can be converted to one of the most useful forms of energy, that is, electricity.[1] The reverse also is important, that is, applying an electric field generates a deformation of the lattice. The former phenomenon is entitled as direct piezoelectric effect, and the latter, converse piezoelectric effect. The atomic origin of piezoelectricity is centered on asymmetric charge distributions generated by anisotropic bonding between cationic and anionic species. In homogeneous bulk crystals, the charge asymmetry strictly requires noncentrosymmetric atomic lattice structures, but interfaces, defects, and strain gradients can also induce piezoelectricity in symmetric crystals.[2] Creating piezoelectricity in technologically important materials, such as silicon and 2D layered semiconductors, potentially enables integrated nanoelectromechanical system (NEMS) devices, including radios, switches, tweezers, and mass, and gas sensors.[3] Previously, giant electromechanical coupling and pyroelectric figure of merit were discovered in the 2D interface between bulk, nonpiezoelectric metal and oxide. However, the effect of 1D interfaces between 2D materials to piezoelectricity has never been experimentally studied. The question is fundamentally interesting as well because 2D materials often show totally different physical characteristics from their bulk counterparts.[4]

Several layered 2D materials like MoS_2, which possess inversion symmetry in their bulk phases lack centrosymmetry in the monolayer limit. Such inversion symmetry breaking on the monolayer 2D materials enables nonlinear optical properties and valley-selectivity.[5] Therefore, there has been a lot of interest in investigating in-plane piezoelectricity in 2D layered materials.[6,7] However, such theoretical and experimental investigations have thus far been limited to homogeneous single-phase 2D materials like transition metal dichalcogenides (MoS_2,[8] WSe_2,[9] $MoTe_2$[6]), monochalcogenides (SnS[10,11]), C/N-based materials (hBN,[12] g-C3N[13]), 2D elements (Se[14]), and ultrathin group III–VI binaries (GaAs, InP,[15] In_2Se_3[16]), etc.

In the few-layer limit, the presence of piezoelectricity often depends on the number layers. Therefore, previous studies have been limited to attempts to engineer this symmetry-breaking behavior by precise growth of an odd number of layers, which requires sophisticated synthesis methods like MBE.[5] In addition, single-phase in-plane piezoelectricity is also limited by edge effects.[17] An alternate way to engineer centrosymmetry in bulk 3D materials is in the form of heterointerfaces, which break inversion symmetry either by the presence of interfacial strain, in-built electric field, or charge transfer.[2,18] This

A. B. Puthirath, X. Zhang, R. Xu, J. Lai, R. Vajtai, V. Swaminathan, H. Zhu, P. M. Ajayan
Department of Materials Science and Nanoengineering
Rice University
Houston, TX 77005, USA
E-mail: anandputhirath@rice.edu; hanyu.zhu@rice.edu; ajayan@rice.edu

A. Krishnamoorthy, P. Vashishta
Department of Physics and Astronomy
University of Southern California
Los Angeles, CA 90089, USA
E-mail: priyav@usc.edu

F. S. Samghabadi, D. Litvinov
Materials Science and Engineering Program
University of Houston
Houston, TX 77204, USA

D. C. Moore, N. R. Glavin
Materials and Manufacturing Directorate
Air Force Research Laboratory
Wright-Patterson AFB, OH 45433, USA

T. Zhang, D. E. Sanchez, F. Zhang, M. Terrones
Materials Science & Engineering
The Pennsylvania State University
University Park, PA 16802, USA

The ORCID identification number(s) for the author(s) of this article can be found under https://doi.org/10.1002/adma.202206425.

DOI: 10.1002/adma.202206425

approach offers several advantages: i) it provides an expanded design space because we have access to multiple materials across the interface to tune the piezoelectricity; and ii) such structures show piezoelectric behavior even in the bulk and not only in thin/monolayer films.

This interfacial engineering strategy has been used to construct reliable out-of-plane piezoelectricity in layered materials by synthesizing Janus monolayers[19] or by engineering van der Waals heterostructures using different layered material combinations such as MoS_2/In_2Se_3.[17] However, such out-of-plane symmetry breaking is usually screened and weakened by the depolarization field. Therefore, there is an attempt to emphasize materials with in-plane polarizations over those exhibiting out-of-plane polarizations because the former prevent depolarization according to electrostatic boundary conditions.[11] Combining these two approaches to engineering in-plane piezoelectricity using 1D lateral heterointerfaces is a novel technique that gives the best of both worlds—in-plane piezoelectricity in few-layer and bulk samples without large depolarization fields (see the schematic provided in **Figure 1**).

In this work, we have grown multilayer 2H–1T′ $MoTe_2$ in-plane homojunctions and demonstrated enhanced piezoelectricity using piezoresponse force microscopy (PFM) supported by first-principal calculations. The mechanical robustness of the junction is enabled by the simultaneous growth of both phases on the same substrate. The piezoresponse amplitude peaks at the homojunction interface, as opposed to a step function expected from noninteracting 2H and 1T′ films. Density functional theory (DFT) calculations successfully reproduced the piezoelectric responses for the 2H phase and 1T′ phase away from the interface and at the interface, which are attributed to the formation of Schottky junction and charge transfer, excessive mechanical stress and charge inhomogeneity that exist at the 2H–1T′ in-plane interface. Our results are promising and pave a pathway toward engineering 2D piezoelectricity at 1D metal-semiconductor junctions.

2. Results and Discussion

We systematically investigate the mechanism underpinning the amplified piezoelectricity observed at the 2H–1T′ in-plane homojunction interface of $MoTe_2$. The preparation of $MoTe_2$ in-plane homojunction is given in the Experimental Section and Section S1, Supporting Information. The formation of in-plane homojunction is validated with the help of Raman spectroscopy, X-ray photoelectron spectroscopy (XPS), transmission electron microscopy (TEM), and Kelvin probe force microscopy (KPFM). The Raman signatures of the 2H and 1T′ phases of $MoTe_2$ are sufficiently distinct, enabling spatial differentiation of the existence of each phase. The out-of-plane Raman-active mode A_{1g} (≈172 cm^{-1}) and in-plane mode $E_{2g}{}^1$ (≈232 cm^{-1}) are observed in the 2H $MoTe_2$ region and Raman bands such as A_u(≈108 cm^{-1}), A_g (≈127 cm^{-1}), B_g (≈161 cm^{-1}), and A_g (≈256 cm^{-1}, second order peak) are observed in the 1T′ phase Raman spectrum (**Figure 2**a).[20] The presence of all of the Raman bands in the respective regions imply the simultaneous growth of both 2H and 1T′ $MoTe_2$ over Si/SiO_2. Among the set of Raman bands observed in 2H and 1T′ phases, in-plane modes including $E_{2g}{}^1$ (≈232 $cm^{-1,}$ 2H phases) and B_g (≈161 cm^{-1} 1T′ Phase) are seen to be more intense confirming the 2D confinement in the grown samples.[21] It is all also interesting to note that the dominant peaks of one phase are absent or feebly present in the other phase indicating the phase purity and homogeneity of each region. To examine the nature of 2H/1T′ $MoTe_2$ homojunction, Raman intensity mapping is attempted across the interface region seen in the optical microscopy image. Within the square region of 50 × 50 μm^2 (Figure 2b), the collected Raman spectrum from the bottom region exclusively shows 2H $MoTe_2$ peaks while the top shows just 1T′ $MoTe_2$ bands. The Raman bands used for the mapping are $E_{2g}{}^1$ mode at 232 cm^{-1} and B_g mode at 161 cm^{-1} for the 2H phase and 1T′ $MoTe_2$ phase, respectively. The Raman mapped image (Figure 2b, right) displays the spatial spreading of 2H/1T′ $MoTe_2$ homojunction, though the resolution is limited to few micrometers to vividly describe the diffusivity of each phase into the other phase, if any. The optical dielectric constants of 2H and 1T′ phases are recorded and provided in Section S2, Supporting Information, which helps differentiate and prove the presence of both phases in the grown samples. The chemical purity and stoichiometry of the two $MoTe_2$ phases were analyzed through X-ray photoelectron spectroscopy. The major peaks observed in the 2H phase region high resolution spectra are 228.5 eV (Mo $3d_{5/2}$), 231.6 eV (Mo $3d_{3/2}$), 573.1 eV (Te $3d_{5/2}$),

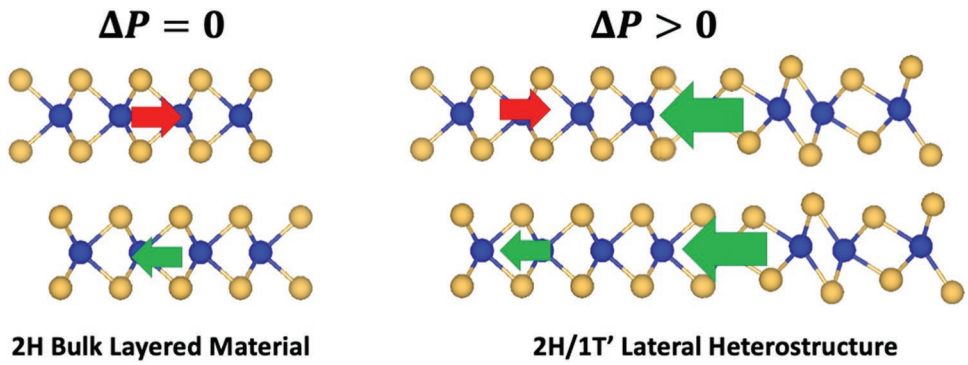

Figure 1. Bulk layered materials (2H phase) regain their center of symmetry and lose their piezoelectric behavior while a lateral heterojunction is capable of retaining the charge asymmetry and hence piezoelectric behavior both in atomically thin and thick films, thereby opening opportunities to bring thickness-independent yet giant piezoelectric responses at 1D interface.

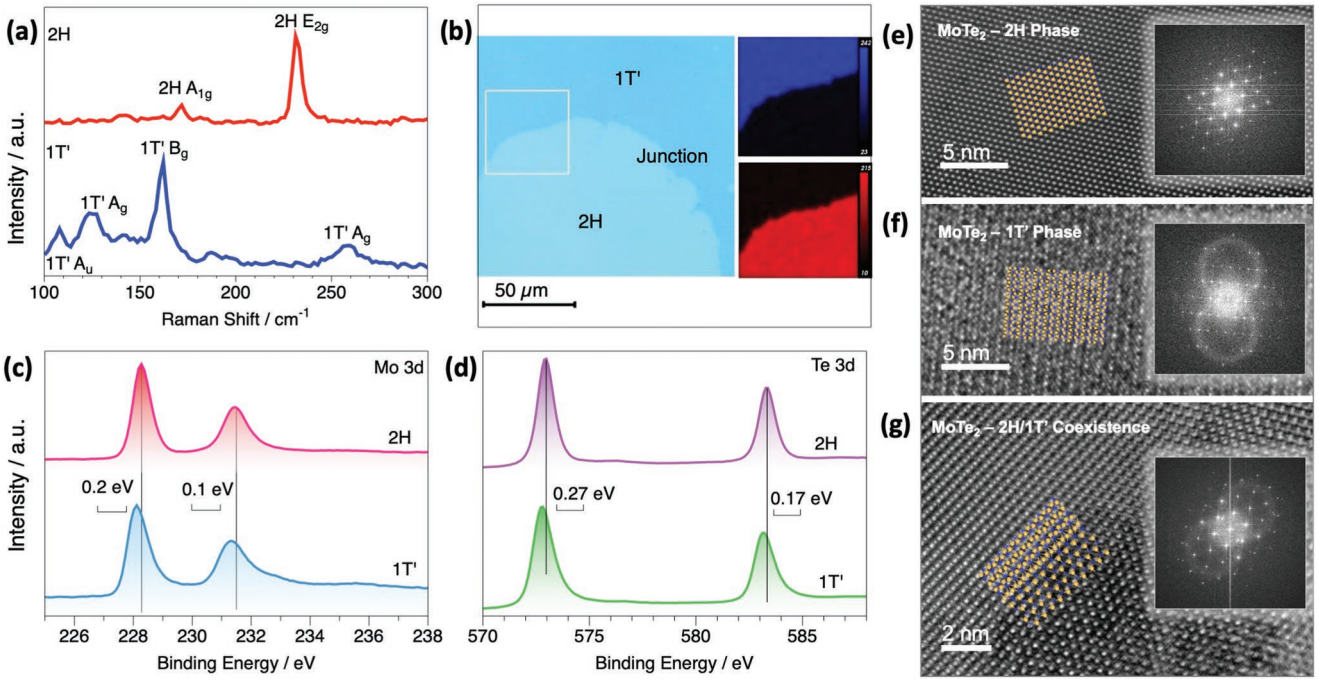

Figure 2. Structural characterizations of in-plane $MoTe_2$ homojunctions. a) Raman spectra of 2H and 1T′ regions. b) Optical microscopy image (left) where the 2H and 1T′ regions can be identified as they show different contrasts, and Raman mapping (right) of 2H and 1T′ areas based on 235 and 160 cm^{-1} bands respectively. c) High-resolution X-ray photoelectron spectra of Mo 3d lines corresponds to 2H and 1T′ phases of $MoTe_2$. A redshift in binding energy of the order of 0.2 eV is observed for the 1T′ phase in comparison to the 2H phase. d) A similar redshift is also observed in Te high-resolution spectra. e–g) High-magnification TEM images of 2H and 1T′ phases and in-plane homojunctions with the FFT pattern in the inset and the superimposed DFT modeled structures are also depicted.

and 583.5 eV (Te $3d_{3/2}$) (Figure 2c,d).[22] The main peaks seen for 1T′ phase are at 228.1 eV (Mo $3d_{5/2}$), 231.3 eV (Mo $3d_{3/2}$), 572.8 eV (Te $3d_{5/2}$), and 583.1 eV (Te $3d_{3/2}$) (Figure 2).[23] Here, the 2H phase has shown slightly higher binding energy than the 1T′ phase. When looking at the atomic ratio of Mo and Te, 1:2.1 is expected for 2H $MoTe_2$, and 1:1.9 is for 1T′ $MoTe_2$. The atomic percentages derived from the survey spectrum follow the same trend for each phase with a slight Te deficiency in the 1T phase. The microstructure and crystallographic orientations of grown $MoTe_2$ samples are studied with high-resolution transmission electron microscopy (HRTEM). The HRTEM images and their fast Fourier transforms (FFT) are displayed in Figure 2e–g. The DFT modeled structures are also superimposed on the corresponding phases. The 2H region shows (Figure 2e) a hexagonal crystal structure while 1T′ is monoclinic (Figure 2f). The most important region, that is, the interface, is further examined with the help of aberration-corrected scanning transmission electron microscopy. The lower part of Figure 2g shows the image of interface region where 2H phase and 1T′ phases can be apparently differentiated with a smooth and robust interface region.

The in-plane 2H–1T′ $MoTe_2$ homojunctions are further examined using Kelvin probe force microscopy (KPFM). The reference image seen in the optical microscopy image (**Figure 3**a) clearly identifies the 2H and 1T′ $MoTe_2$ domains by their differing contrasts where the inner circular area is composed of 2H phase and the outer area with 1T′ $MoTe_2$. The AFM height image and the height line profiles show no significant variation in the heights across in-plane 2H–1T′ $MoTe_2$ junctions (Figure 3b,c). KPFM measures the contact potential difference (CPD) between the material and the tip. The values $[\Phi(\text{tip}) - \Phi(1T'\ MoTe_2)]/e$ and $[\Phi(\text{tip}) - \Phi(2H\ MoTe_2)]/e$, where Φ(tip), $\Phi(1T'\ MoTe_2)$, and $\Phi(2H\ MoTe_2)$, are the work functions for the tip, 1T′ $MoTe_2$, and 2H $MoTe_2$, respectively, define the CPDs on 1T′ and 2H domains of $MoTe_2$. Thus, the work function difference between the 2H and 1T′ $MoTe_2$ phases, $\Phi(2H\ MoTe_2) - \Phi(1T'\ MoTe_2)$, can be computed. A KPFM image and the potential line profiles across the homojunction region confirm a sharp 30 mV potential difference between the 2H and 1T′ $MoTe_2$ domains (Figure 3d,e). The work function difference can be described in terms of the Te deficiency in 1T′ $MoTe_2$ and the electronic band structure difference between the 2H and 1T′ $MoTe_2$ phases. The derived average spread value is around 2.44 μm. Extended KPFM results are provided in the Section S4, Supporting Information. To precisely define the spatial spread of the effect of homojunction, simulations are performed on an extended simulation cell of lateral dimensions 123 Å × 7 Å, containing 80 formula units of $MoTe_2$ (40 units of 2H $MoTe_2$ and 40 units of 1T′ $MoTe_2$). Charge redistribution at the H–T′ $MoTe_2$ interface, depicted here (Figure 3f) as the difference in the charge density of the H–T′ interfacial system and the individual parent phases, provides a definition of the interfacial width. The majority of the charge redistribution is confined to within 9 Å of the interface, which is generally lower than the resolution of the surface probe microscopy (SPM) scans. Variation in the local potential (sum of ionic potential, Hartree potential and exchange correlation potential) across the H–T′ $MoTe_2$ interfaceis displayed in Figure 3g. Bending in the

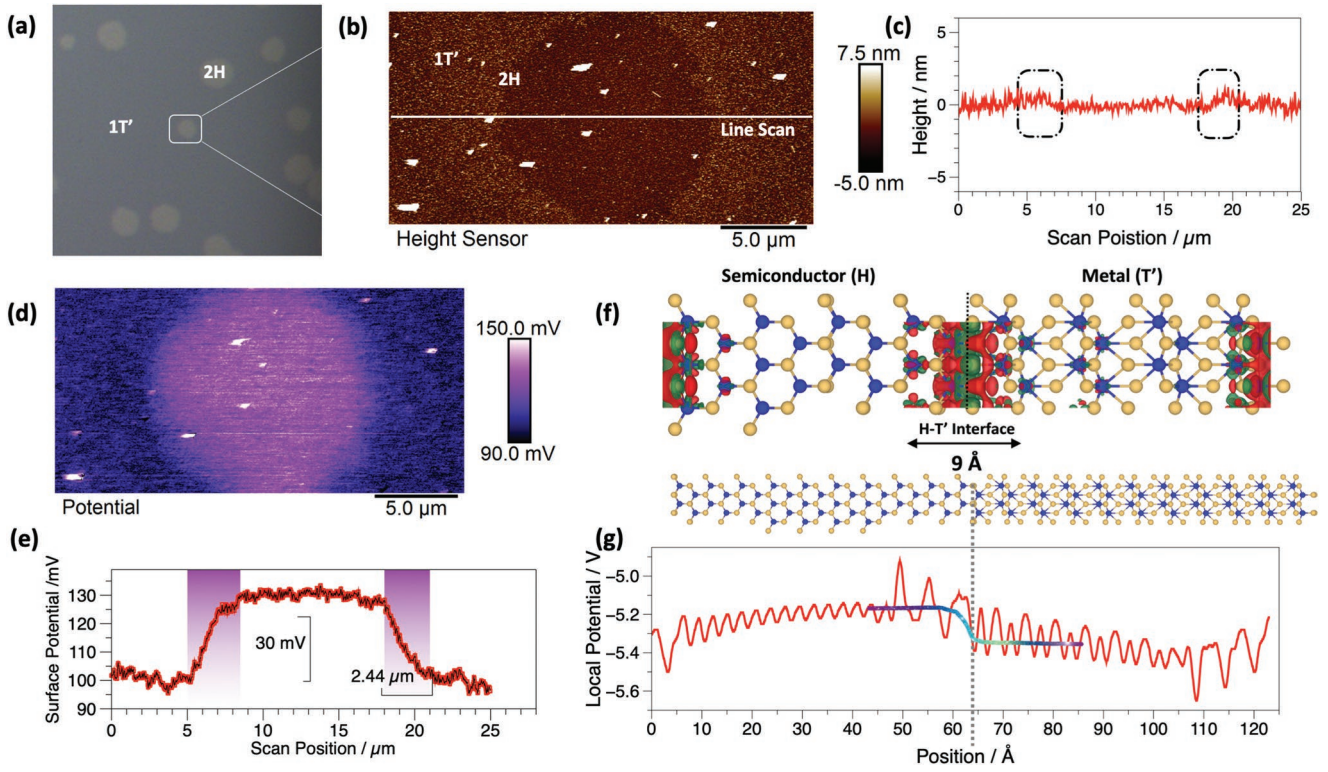

Figure 3. KPFM measurement of 2H/1T′ $MoTe_2$ in-plane homojunctions. a) Optical microscopy image, b) AFM height image, and c) height line profile. d) KPFM potential map of the 2H/1T′ interface. e) Potential profile of (red line) a single line and (black line) the twenty lines averaged in (d). f) Charge redistribution at the H–T′ $MoTe_2$ interface, (color codes-red: electron-deficient, green: electron-rich, blue: Mo atom, cream: Te atom). g) Variation in the local potential across the H–T′ $MoTe_2$ interface.

local potential (responsible for band bending) is observed at both H–T′ interfaces located at $x = 0$ and $x = 64$ Å (3g).

To detect piezoelectricity in the as grown atomically thin $MoTe_2$ homojunctions, we measure the electric-field induced surface deformation using a dual AC resonance tracking (DART)-PFM scheme.[24] The field is locally applied by a conductive contact probe, and the electromechanical deformation at the surface of atomically thin and flat materials is sensed as the first harmonic component of the probe's deflection. The deflection amplitude is proportional to the converse piezoelectric coefficient and enhanced by the mechanical resonance of the probe. Although the probe is primarily sensitive to the out-of-plane electromechanical motion, an in-plane piezoresponse along the cantilever's direction can also be projected to the vertical deflection of the cantilever.[25] The contribution of in-plane and out-of-plane piezoresponse may thus be distinguished by different cantilever orientations with respect to the sample (**Figure 4**a). Figure 4b shows the scanning image of topography for a typical $MoTe_2$ homojunction, where the 1D interface is parallel to the cantilever. The corresponding optical microscopy image of the sample under the PFM cantilever is provided in Section S5.1, Supporting Information. From the topography we found a small apparent height difference of <2 nm across the 2H–1T′ homojunction (Figure 4b,c,f) compared with the total sample thickness of 10 nm. This apparent step is likely due to the difference in probe-sample interaction for the two phases. From the amplitudes and phases of the DART-PFM measurement (Figure 4d and Section S5.2a,b, Supporting Information), we may calculate the apparent electromechanical motion of the sample (Figure 4d).[26] The insulating 2H phase shows very weak piezoresponse, as expected from the crystalline centrosymmetry. The semimetallic 1T′ phase shows finite piezoresponse that likely comes from the capacitive force due to electrostatic contact potential.[26] The PFM signal's transition between the 2H and 1T′ is smooth, agreeing with the electrostatic potential map (Figure 3). Surprisingly, when the 1D interface is rotated to be nearly perpendicular to the cantilever, an enhanced piezoresponse emerges at the junction (Figure 4e,f). The difference between the two cantilever orientations indicates that the probe picks up an in-plane force exerted by the sample under the applied electric field. Although the apparent amplitude of electromechanical coupling is around 2 pm V^{-1} at the interface when subtracting the background piezoresponse from 1T′ after considering the resonance enhancement factor, Figure 4g, the measured coupling is only the partial projection of the actual in-plane piezoelectricity. This peak cannot be removed by applying any tip bias, and bears no resemblance to the KPFM profile, ruling out pure electrostatic effect.[27] It is impressive that, a few unit cells at the interface are piezoelectric active and can produce large deformation that can be resolved in the SPM methods like piezoelectric force microscopy.

To understand the origin of the amplified piezoelectric effect near the 2H–1T′ $MoTe_2$ interface, we performed ab initio simulations of 2H, 1T′, and in-plane 2H–1T′ $MoTe_2$ homostructures. Specifically, we calculate the in-plane piezoelectric coefficient

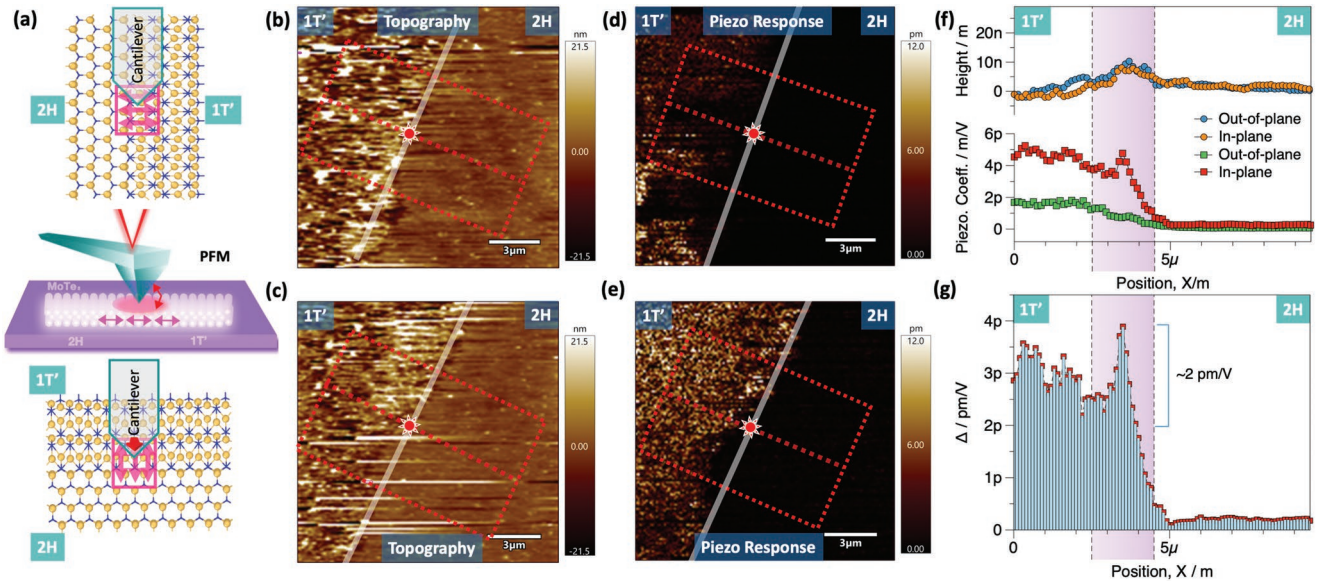

Figure 4. PFM measurement of 2H/1T′ $MoTe_2$ in-plane homojunction. a) Illustration of the coupling between the in-plane piezoresponse of the sample (pink arrow) and the out-of-plane deflection of the cantilever (red arrow) depending on the orientation of the 1D boundary with respect to the cantilever. b,c) Topography, c,d) piezoresponse images corresponding cross-sections of the homojunction when the cantilever is aligned (out-of-plane) with the 2H–1T′ boundary and nearly perpendicular (in-plane) to the 2H–1T′ boundary. f) (top) A small height difference in topography for 2H and 1T′ regions due to the difference in tip–sample interaction allows us to accurately determine the phase boundary labeled with thick white shaded line. f) (bottom) And when comparing the piezoelectric coefficient profile across the junction for different configurations, an additional peak is observed in the averaged piezoresponse cross-section at the boundary for in-plane orientation revealing the amplified piezoelectricity due to the presence of polar charges at the interface. g) The modulation in the PFM coefficient value is visualized by drawing the difference between in-plane and out-of-plane configurations which is ≈2 pm V^{-1}.

(d_{11}) in these three structures as a ratio between the observed change in total polarization (ΔP) and lattice stress ($\Delta\sigma$) in response to an infinitesimal lattice strain (ε_{11}). **Figure 5**a,b shows the computed change in charge densities in the 2H (1T′) crystal structure due to the application of 1% in-plane lattice strain.

The relatively symmetric nature of charge redistribution due to lattice strain reflects a relatively minor change in the overall polarization of lattice and the correspondingly low value of the piezoelectric coefficient, d_{11} = 3.02 pm V^{-1} (d_{11} = 0.19 pm V^{-1}). In contrast, when the same lattice strain is applied to the low-energy atomically sharp α type interface[28,29] between the 2H

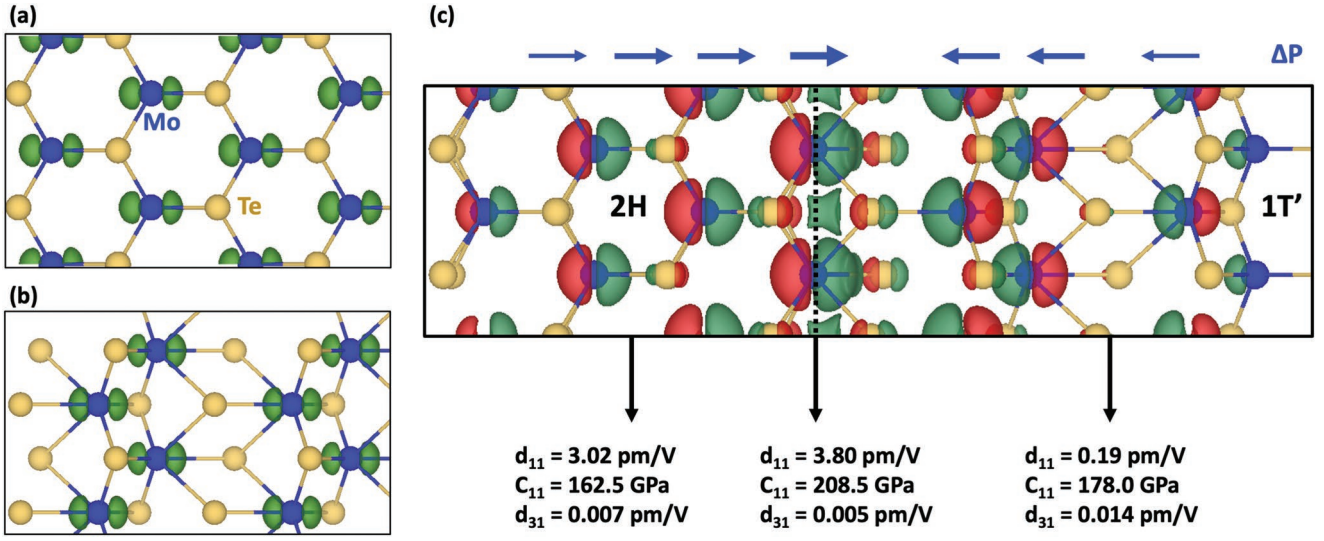

Figure 5. a,b) Redistribution of electron densities in the H and T′ $MoTe_2$ structure due to the application of ε_{xx} = 0.01. c) Extensive redistribution of electron densities due to 1% lattice strain at the H–T′ interface leads to local dipoles from more electron-deficient (red) to electron-rich (green) regions. The redistribution is greatest at the interface and decreases with distance from the interface. The interfacial region has both enhanced piezoelectric coefficient (d_{11}) and elastic modulus (C_{11}) relative to the parent H and T′ phases.

Table 1. Change in Bader charges of Mo and Te atoms in 2H, 1T′, and 2H–1T′ interfaces due to application of 1% lattice strain.

System	Mo Δq (e^-)	Te Δq (e^-)
2H $MoTe_2$	−0.009	0.005
1T′ $MoTe_2$	−0.011	0.008
2H–1T′ interface	−0.17	0.13

and 1T′ phases of $MoTe_2$, we observe a considerable redistribution of charge densities and the formation of finite local dipole moments, similar to those observed in semiconductor–metal Schottky junctions.[2] This redistribution of charge densities and the corresponding local dipole is strongest closest to the interface and decays with distance away from the interface. This large change in polarization is responsible for a large value of the measured polarization coefficient, $d_{11} = 3.80$ pm V^{-1} for the region close to the 2H/1T′ interface. Similar enhancement of piezoelectric coefficients at the 2H–1T′ interface is also observed in bilayer and bulk-like simulation cells containing lateral homointerfaces between multiple 2H/1T′ layers (see Section S6, Supporting Information). Besides, we have also investigated the d_{31} coefficient values, but they are very small for both the individual parent phases and at the interface.

We also performed Bader charge analysis to quantify this larger charge transfer in the interfacial system relative to the parent 2H and 1T′ phases. **Table 1** shows the computed change in Bader charge densities for Mo and Te atoms in the 2H, 1T′ and interfacial structures due to the application of 1% lattice stain. Consistent with the charge redistribution map seen in Figure 5a,b, we notice that the transfer of charge between atoms across the interface is of one order of magnitude larger than that measured in the parent 2H and 1T′ phases. The computed charge densities for unstrained and 1% tensile strained 2H, 1T′ monolayer $MoTe_2$ as well as monolayer $MoTe_2$ interface between 2H and 1T′ is provided in Section S7, Supporting Information.

While the observation of an improved piezoelectric response due to doping and alloying is relatively well known, such effects are accompanied by a softening of the crystal lattice. In contrast, in this charge-transfer-based piezoelectric material, we notice an improvement in piezoelectric coefficient along with a simultaneous improvement in stiffness since the computed interfacial elastic modulus ($C_{11} = 208.5$ GPa) is larger than that of the parent phases H (162.5 GPa) and T′ (178.0 GPa). This is consistent with similar observations in other H/T′ and H/T TMDC interfaces.[30,31] The hardness and reduced modulus values of the 2H and 1T′ phases are experimentally measured through nanoindentation experiments and the results, appended in the Section S8, Supporting Information, are found to be the theoretical values.

3. Conclusion

We have investigated, arguably for the first time, the influence of 1D yet atomically thin and sharp interfaces on the electromechanical properties of materials with 2H–1T′ $MoTe_2$ semiconductor–metallic homojunction as a case study. We have successfully grown the 10 nm-thick 2H–1T′ $MoTe_2$ homojunction via chemical vapor deposition and characterized the formation of homojunctions and the phase purity through Raman, XPS, TEM, ellipsometry, Kelvin probe microscopy, and nanoindentation. The piezoelectric property of the 2H, 1T′ and the homojunctions are investigated via piezoresponse force microscopy which showed an amplified piezoelectric response at the junction that converges to a stable low piezoresponse toward the semiconducting 2H phase and nonzero response toward the conducting 1T′ phase due to capacitive effects. The density functional theory calculations suggest that the enhanced piezoelectricity observed at the 2D material interface (1D junction) is due to the charge transfer across the semiconducting (2H) and metallic (1T′) junction which resulted in the formation of dipoles and excess charge density. Unlike the conventional approaches such as doping and alloying that are usually accompanied by the softening of the crystal lattice, we observed a stronger piezoelectric response with an improvement in the stiffness of the materials. The discovery of giant piezoresponse at 1D metal–semiconductor junctions may pave the way for realizing NEMS with desirable form factors using existing yet cost-effective fabrication methodologies like CVD and PVD.

4. Experimental Section

Synthesis: Molybdenum (Mo) films (3 nm) were deposited to a cleaned SiO_2/Si substrate via e-beam evaporation of Mo. Later, the sample was tellurized inside a furnace by keeping the Te powder upstream relative to the 50 SCCM Ar/H_2 (15%) gas flow. After purging the carrier gas for 20 min, the CVD furnace was warmed toward the reaction temperature (50 °C min^{-1}). The temperature was maintained at 750 °C for a specific duration of growth before cooling down to 500 °C and later the lid of the furnace was opened to upsurge the rate of cooling. More details have been reported elsewhere.[32]

Characterization: A Renishaw inVia micro spectrometer was used to record the Raman spectra and the spatial maps of the samples. 532 nm laser light with 10% intensity was used to excite the samples. A PHI Quantera II with monochromatic Al Kα X-rays was employed to collect the XPS spectra of the samples at 148.6 and 26 eV pass energy. TEM sample was prepared by PMMA-assisted transfer method. High-resolution TEM was performed using a FEI Titan G2 60–300 microscope, operated at 80 kV, offering sub-angstrom image resolution. KPFM was performed on a Bruker Dimension Icon in PeakForce KPFM (frequency modulated) mode using a PFQNE-AL probe. Values over the 2H, 1T′ and junction region were then averaged. Atomic force microscopy and piezoresponse force microscopy were performed with an ASYLUM Research probe model "ASYELEC-01-R2" with a silicon tip coated with Ti/Ir (5/20). The spring constant and lever air resonance frequency of the probe are 2.8 N m^{-1} and 75 kHz, respectively. The resonance frequency of the tip during measurement was 330 kHz on average. A Hysitron TI 980 Tribo Indenter with Berkovich Probe of radius of curvature 150 nm was used to measure the micromechanical properties where a quasi-load function (max load: 200 μN) was employed for a single indentation.

Computational: Ground-state energies of the optimized interfacial structures and bulk crystal supercells were obtained from DFT performed using the projector augmented wave[33] method implemented in VASP, the Vienna Ab initio Simulation Package.[34,35] The B3LYP hybrid exchange-correlation function was used for all simulations.[36,37] Electron wavefunctions were expanded in a plane-wave basis set with an energy cut-off of 750 eV. The reciprocal space was sampled only at the Γ point in the Brillouin zone with 0.1 eV Gaussian smearing of orbital occupancies.

Simulations of 2H–1T′ lateral interfaces were performed on 48-atom supercells, containing eight formula units each of 2H and 1T′ $MoTe_2$, in a simulation cell measuring 24.75 Å × 6.97 Å along the

a- and *b*-directions. DFT simulations of monolayer 2H and 1T′ $MoTe_2$ crystals were performed on supercells comprising $4 \times 2 \times 1$ unit cells of 2H and $2 \times 2 \times 1$ unit cells of 1T′ $MoTe_2$, each containing 24 atoms. Periodic images of these supercells were separated by 10 Å along the *c*-axis to remove artificial image interactions. Self-consistency cycle were continued until the energy was converged to within 1×10^{-5} eV per atom and forces on all ions were below 5×10^{-2} eV $Å^{-1}$. Macroscopic electronic polarization in all systems was computed using Berry phase expressions in accordance with the modern theory of polarization implemented in VASP.[38–41] Bader charge analysis was performed using the fast Bader charge analysis program developed by the Henkelman.[42,43] All crystal and interfacial structures in this study were visualized using the VESTA3 crystal structure program.[43]

Supporting Information

Supporting Information is available from the Wiley Online Library or from the author.

Acknowledgements

This material is based upon work supported by the Air Force Office of Scientific Research under award number FA9550-18-1-0072 (P.M.A., A.B.P., X.Z., and J.L.). Microscopy research performed at PSU. N.G. thanks the support of Air Force Office of Scientific Research grant FA9550-19RYCOR050. H.Z. acknowledges the support by the National Science Foundation (NSF) under award number DMR-2005096.

Conflict of Interest

The authors declare no conflict of interest.

Authors Contribution

A.B.P., X.Z., A.K., and R.X. contributed equally to this work. A.B.P. and P.M.A. designed and executed the project. A.B.P. wrote the manuscript with the help of A.K., X.Z., R.X., F.S.S., and H.Z. X.Z. synthesized the samples and carried out basic characterizations with J.L. T.Z., D.E.S., F.Z., and M.T. performed HR-TEM experiments and analysis. D.C.M. and N.R.G. carried out KPFM experiments. F.S.S., A.B.P., and R.X. carried out PFM imaging and analysis advised by H.Z. A.K. and P.V. performed the theoretical calculations and modeling. V.S., H.Z., and R.V. joined for the discussion and analysis. All the authors contributed to writing the manuscript.

Data Availability Statement

TThe data that support the findings of this study are available from the corresponding author upon reasonable request.

Keywords

2D materials, in-plane homojunctions, molybdenum(IV) telluride, piezoelectricity, Schottky junctions

Received: July 15, 2022
Revised: August 2, 2022
Published online:

[1] W. P. Mason, *J. Acoust. Soc. Am.* **1981**, *70*, 1561.
[2] M.-M. Yang, Z.-D. Luo, Z. Mi, J. Zhao, S. Pai E, M. Alexe, *Nature* **2020**, *584*, 377.
[3] X. Fan, A D. Smith, F. Forsberg, S. Wagner, S. Schröder, S. S. A. Akbari, A C. Fischer, L. G. Villanueva, M C. Lemme, F. Niklaus, *Microsyst. Nanoeng.* **2020**, *6*, 17.
[4] P. Rodgers, J. Heath, *Nanoscience and Technology: A Collection of Reviews from Nature Journals*, World Scientific, Singapore **2009**.
[5] J. Nordlander, M D. Rossell, M. Campanini, M. Fiebig, M. Trassin, *Nano Lett.* **2021**, *21*, 2780.
[6] S. Yuan, X. Luo, H. L. Chan, C. Xiao, Y. Dai, M. Xie, J. Hao, *Nat. Commun.* **2019**, *10*, 1775.
[7] R. Hinchet, U. Khan, C. Falconi, S.-W. Kim, *Mater. Today* **2018**, *21*, 611.
[8] W. Wu, L. Wang, Y. Li, F. Zhang, L. Lin, S. Niu, D. Chenet, X. Zhang, Y. Hao, T. F. Heinz, J. Hone, Z. L. Wang, *Nature* **2014**, *514*, 470.
[9] J.-H. Lee, J. Y. Park, E. B. Cho, T. Y. Kim, S. A. Han, T.-H. Kim, Y. Liu, S. K. Kim, C. J. Roh, H.-J. Yoon, H. Ryu, W. Seung, J. S. Lee, J. Lee, S.-W. Kim, *Adv. Mater.* **2017**, *29*, 1606667.
[10] H. Khan, N. Mahmood, A. Zavabeti, A. Elbourne, Md. A Rahman, B. Y. Zhang, V. Krishnamurthi, P. Atkin, M B. Ghasemian, J. Yang, G. Zheng, A R. Ravindran, S. Walia, L. Wang, S P. Russo, T. Daeneke, Y. Li, K. Kalantar-Zadeh, *Nat. Commun.* **2020**, *11*, 3449.
[11] N. Higashitarumizu, H. Kawamoto, C.-J. Lee, B.-H. Lin, F.-H. Chu, I. Yonemori, T. Nishimura, K. Wakabayashi, W.-H. Chang, K. Nagashio, *Nat. Commun.* **2020**, *11*, 2428.
[12] G.-J. Lee, M.-K. Lee, J.-J. Park, D. Y. Hyeon, C. K. Jeong, K.-I. Park, *ACS Appl. Mater. Interfaces* **2019**, *11*, 37920.
[13] M. Zelisko, Y. Hanlumyuang, S. Yang, Y. Liu, C. Lei, J. Li, P. M. Ajayan, P. Sharma, *Nat. Commun.* **2014**, *5*, 4284.
[14] M. Wu, Y. Wang, S. Gao, R. Wang, C. Ma, Z. Tang, N. Bao, W. Wu, F. Fan, W. Wu, *Nano Energy* **2019**, *56*, 693.
[15] C. J. Cui, F. Xue, W. J. Hu, L. J. Li, *npj 2D Mater. Appl.* **2018**, *2*, 18.
[16] Y. Zhou, D. Wu, Y. Zhu, Y. Cho, Q. He, X. Yang, K. Herrera, Z. Chu, Y. Han, M. C. Downer, H. Peng, K. Lai, *Nano Lett.* **2017**, *17*, 5508.
[17] S. Yuan, W. F. Io, J. Mao, Y. Chen, X. Luo, J. Hao, *ACS Appl. Nano Mater.* **2020**, *3*, 11979.
[18] N. Mahmood, H. Khan, K. Tran, P. Kuppe, A. Zavabeti, P. Atkin, M. B. Ghasemian, J. Yang, C. Xu, S. A. Tawfik, M. J. S. Spencer, J. Z. Ou, K. Khoshmanesh, C. F. McConville, Y. Li, K. Kalantar-Zadeh, *Mater. Today* **2021**, *44*, 69.
[19] A.-Y. Lu, H. Zhu, J. Xiao, C.-P. Chuu, Y. Han, M.-H. Chiu, C.-C. Cheng, C.-W. Yang, K.-H. Wei, Y. Yang, Y. Wang, D. Sokaras, D. Nordlund, P. Yang, D A. Muller, M.-Y. Chou, X. Zhang, L.-J. Li, *Nat. Nanotechnol.* **2017**, *12*, 744.
[20] X.-J. Yan, Y.-Y. Lv, L. Li, X. Li, S.-H. Yao, Y.-B. Chen, X.-P. Liu, H. Lu, M.-H. Lu, Y.-F. Chen, *npj Quantum Mater.* **2017**, *2*, 31.
[21] M. Grzeszczyk, M. Zinkiewicz, K. Nogajewski, M. R. Molas, M. Potemski, *2D Mater.* **2016**, *3*, 025010.
[22] L. Zhou, K. Xu, A. Zubair, A D. Liao, W. Fang, F. Ouyang, Yi-H Lee, K. Ueno, R. Saito, T. Palacios, J. Kong, M S. Dresselhaus, *J. Am. Chem. Soc.* **2015**, *137*, 11892.
[23] C. H. Naylor, W. M. Parkin, J. Ping, Z. Gao, Y. R. Zhou, Y. Kim, F. Streller, R. W. Carpick, A. M. Rappe, J. M. Kikkawa, A. T. C. Johnson, *Nano Lett.* **2016**, *16*, 4297.
[24] J. A. Christman, R. R. Woolcott, A. I. Kingon, R. J. Nemanich, *Appl. Phys. Lett.* **1998**, *73*, 3851.
[25] S. V. Kalinin, B. J. Rodriguez, S. Jesse, J. Shin, A P. Baddorf, P. Gupta, H. Jain, D. B. Williams, A. Gruverman, *Microsc. Microanal.* **2006**, *12*, 206.
[26] B. J. Rodriguez, C. Callahan, S. V. Kalinin, R. Proksch, *Nanotechnology* **2007**, *18*, 475504.
[27] N. Balke, P. Maksymovych, S. Jesse, I. I. Kravchenko, Q. Li, S. V. Kalinin, *ACS Nano* **2014**, *8*, 10229.

[28] A. Apte, A. Krishnamoorthy, J. A. Hachtel, S. Susarla, J. Yoon, L. M. Sassi, P. Bharadwaj, J. M. Tour, J. C. Idrobo, R. K. Kalia, A. Nakano, P. Vashishta, C. S. Tiwary, P. M. Ajayan, *Nano Lett.* **2019**, *19*, 6338.
[29] Y.-C. Lin, D. O. Dumcenco, Y.-S. Huang, K. Suenaga, *Nat. Nanotechnol.* **2014**, 391.
[30] A. Apte, V. Kochat, P. Rajak, A. Krishnamoorthy, P. Manimunda, J. A. Hachtel, J. C. Idrobo, S. A. Syed Amanulla, P. Vashishta, A. Nakano, R. K. Kalia, C. S. Tiwary, P. M. Ajayan, *ACS Nano* **2018**, *12*, 3468.
[31] B. Mortazavi, A. Ostadhossein, T. Rabczuk, A. C. T. Van Duin, *Phys. Chem. Chem. Phys.* **2016**, *18*, 23695.
[32] X. Zhang, Z. Jin, L. Wang, J. A. Hachtel, E. Villarreal, Z. Wang, T. Ha, Y. Nakanishi, C. S. Tiwary, J. Lai, L. Dong, J. Yang, R. Vajtai, E. Ringe, J. C. Idrobo, B. I. Yakobson, J. Lou, V. Gambin, R. Koltun, P. M. Ajayan, *ACS Appl. Mater. Interfaces* **2019**, *11*, 12777.
[33] P. E. Blöchl, *Phys. Rev. B* **1994**, *50*, 17953.
[34] G. Kresse, J. Furthmüller, *Phys. Rev. B: Condens. Matter Mater. Phys.* **1996**, *54*, 11169.
[35] G. Kresse, J. Furthmüller, *Comput. Mater. Sci.* **1996**, *6*, 15.
[36] C. Lee, W. Yang, R. G. Parr, *Phys. Rev. B* **1988**, *37*, 785.
[37] A. D. Becke, *J. Chem. Phys.* **1993**, *98*, 5648.
[38] R. D. King-Smith, D. Vanderbilt, *Phys. Rev. B* **1993**, *47*, 1651.
[39] R. Resta, *Ferroelectrics* **1992**, *136*, 51.
[40] R. Resta, *Rev. Mod. Phys.* **1994**, *66*, 899.
[41] W. Tang, E. Sanville, G. Henkelman, *J. Phys. Condens. Matter* **2009**, *21*, 084204.
[42] E. Sanville, S D. Kenny, R. Smith, G. Henkelman, *J. Comput. Chem.* **2007**, *28*, 899.
[43] K. Momma, F. Izumi, *J. Appl. Crystallogr.* **2011**, *44*, 1272.